Research Article

Yunlin Le, Jia She*, Jianjun Mao, Xuerui Jing, Jijun Yang, Xianfang Meng, Jun Tan*, Lu Wu*, Wei Zhang, Wenchao Yang*, Xingzhi Pang, and Fusheng Pan

Novel integrated structure and function of Mg–Gd neutron shielding materials

https://doi.org/10.1515/ntrev-2024-0007
received December 1, 2023; accepted March 11, 2024

Abstract: As the lightest metal structural materials, magnesium (Mg) alloys offer extensive application potential. Gadolinium (Gd), as the primary alloying element in Mg alloys and recognized for its notable thermal neutron capture cross-section, is considered one of the most efficient neutron absorbers. Thus, the Mg–Gd alloy is highly expected to emerge as a material with remarkable neutron absorption capacity. Hence, in this study, the thermal neutron-shielding capabilities of Mg–Gd alloys were comprehensively examined by fabricating four as-cast Mg–*x*Gd alloys with varying compositions (x = 0, 5, 10, and 15 wt%). The obtained results were further corroborated by sophisticated modeling and calculations using SuperMC. The results revealed a direct correlation between the thermal neutron absorption capacity of the Mg–Gd alloys and the increase in Gd content, with a noteworthy neutron attenuation factor of 22.33. Moreover, in an Au ion irradiation experiment conducted at 200°C, the Mg–15Gd alloy exhibited exceptional radiation resistance, with a displacement per atom (dpa) of 10. The matrix and second-phase regions were devoid of any cavity formation. Instead, a finite number of dislocation rings were observed, forming both leaf-like and granular Gd-rich nanoscale precipitates. This study underscores the versatility of Mg–Gd alloys as efficient neutron shielding materials and structural materials tailored for applications demanding radiation resistance in diverse environments.

Keywords: neutron-shielding material, Mg alloy, ion irradiation, superMC

*** Corresponding author: Jia She,** College of Materials Science and Engineering, Chongqing University, Chongqing 400044, China; National Engineering Research Center for Magnesium Alloys, Chongqing University, Chongqing 400044, China; National Key Laboratory of Advanced Casting Technologies, Chongqing University, Chongqing, 400044, China, e-mail: jiashe@foxmail.com
*** Corresponding author: Jun Tan,** College of Materials Science and Engineering, Chongqing University, Chongqing 400044, China; National Engineering Research Center for Magnesium Alloys, Chongqing University, Chongqing 400044, China; National Key Laboratory of Advanced Casting Technologies, Chongqing University, Chongqing, 400044, China, e-mail: jun.tan@cqu.edu.cn
*** Corresponding author: Lu Wu,** The First Research Institute of China, Nuclear Power Research and Design Institute, Chengdu 610005, China, e-mail: wulu1002@qq.com
*** Corresponding author: Wenchao Yang**, School of Resources, Environment and Materials, Guangxi University, Nanning 530004, China, e-mail: ywch053@163.com
Yunlin Le, Xingzhi Pang: School of Resources, Environment and Materials, Guangxi University, Nanning 530004, China
Jianjun Mao, Wei Zhang: The First Research Institute of China, Nuclear Power Research and Design Institute, Chengdu 610005, China
Xuerui Jing, Fusheng Pan: College of Materials Science and Engineering, Chongqing University, Chongqing 400044, China; National Engineering Research Center for Magnesium Alloys, Chongqing University, Chongqing 400044, China; National Key Laboratory of Advanced Casting Technologies, Chongqing University, Chongqing, 400044, China
Jijun Yang: Key Laboratory of Radiation Physics and Technology of Ministry of Education, Institute of Nuclear Science and Technology, Sichuan University, Chengdu 610064, China
Xianfang Meng: Beijing Research Center for Radiation Application, Beijing Key Laboratory of Radiation Advanced Materials, Beijing 100015, China

1 Introduction

Nuclear energy has immense potential and significance as a clean and efficient energy source, with its capabilities extending beyond meeting escalating global energy demands, as it also contributes to mitigating greenhouse gas emissions and combating challenges posed by climate change [1]. The progressive development of nuclear energy has been instrumental in driving scientific and technological advancements and facilitating industrial upgrades, thereby providing critical support for economic growth and societal progress. However, with the continuous evolution of nuclear technology, the requirements for reactor materials have increased [2,3]. Specifically, concerning shielding materials, thermal neutron shielding materials are expected to exhibit characteristics such as low density, high-temperature tolerance, and resistance to aging, as well as the capability to seamlessly integrate neutron moderation and absorption [4,5].

Diverse neutron-shielding materials are currently in use [6]. Boron steel, known for its neutron-weakening function and excellent mechanical properties, is a commonly employed shielding material in radiation protection designs [7]. However, the low solubility of boron in steel poses challenges, with trace amounts (0.001–0.007%) adversely affecting the hardenability of steel. High boron content also compromises the ductility and impact resistance of boron steel, restricting its predominant use in applications such as control rods and spent fuel storage materials [8,9].

Lead boron polyethylene, while offering neutron shielding capabilities, exhibits slightly insufficient mechanical structural performance and limited resistance to high temperatures, radiation, and corrosion. Consequently, they are primarily used as single functional material [10]. Recent studies have demonstrated that epoxy resin composites incorporating B or W exhibit exceptional thermal stability and long-term radiation resistance at a low cost. As a result, these composites have extensive applications in radiation shielding; however, they are unsuitable for use as structural materials [11,12]. Additionally, the neutron absorption cross-section of B^{11}, a transmutation product of boron after neutron absorption, sharply decreases over time, rendering materials containing boron less effective in high-dose neutron environments [13]. Concrete, characterized by its adjustable composition, cost-effectiveness, and local availability, is an attractive option for shielding against radiation across various energy segments. However, ordinary concrete has a relatively low density (2.2–2.4 g/cm^3) and limited strength. To enhance the mechanical strength of concrete and its neutron and gamma-ray shielding performance, high-performance or heavy concrete is often formulated by incorporating mineral admixtures or natural/artificial functional coarse aggregates. Despite performance improvements, these formulations result in larger volumes and heavier masses (density 3.0–6.0 g/cm^3) [14,15].

Metal-based materials are an alternative to address these issues. Tungsten, with its effective moderating effect on fast neutrons, achieves 93% shielding of fast neutrons when passing through a 10 cm-thick tungsten plate [16]. As such, tungsten can be used as a shield against secondary high-energy gamma rays produced by neutrons and is an excellent substitute for lead. Some tungsten-containing metal–matrix composites have shielding efficiencies several times higher than that of lead composites [17]. However, the relatively high cost of tungsten has led to the development of tungsten alloys containing Ni, Cu, Co, Mo, and Cr [18]. These alloys, known as high specific gravity alloys (with tungsten mass fractions ranging from 70 to 99%), offer advantages such as a high specific weight, high strength, strong ray absorption capacity, substantial thermal conductivity, good weldability, and processability. Other metals, including hafnium, samarium, and cadmium, have been combined to create neutron and gamma-ray shielding materials [19–21]. However, owing to issues such as source scarcity, high costs, significant secondary radiation yield, and toxicity concerns, these materials are seldom used in practical applications and are gradually being replaced with alternative materials.

Currently, traditional materials such as water, lead, and concrete remain prevalent in the realm of reactor radiation protection. However, these materials exhibit notable limitations and are primarily suited for stationary nuclear power reactors and accelerators where stringent requirements for the weight and volume of shielding materials are typically absent, and cost is the primary consideration. Consequently, researchers are focusing on developing new materials that address these shortcomings by offering high-temperature resistance, excellent mechanical properties, environmental friendliness, non-toxicity, and enhanced neutron absorption capabilities.

The neutron capture cross-section of Mg is widely acknowledged for its moderating properties, while magnesium (Mg) alloys demonstrate exceptional compatibility with both fuel and coolant materials. It possesses several advantages such as low induced radioactivity, high thermal conductivity, and ease of welding. Additionally, it demonstrated strong adaptability to dimensional changes resulting from stress variations caused by thermal cycling and irradiation. Consequently, the neutron capture cross-section of Mg is frequently applied in carbon dioxide gas-cooled reactors and as a shielding material for natural uranium cladding [22]. The combination of Mg alloys with specific rare earth elements can have a unique impact on the field of nuclear energy. Gadolinium (Gd) has a significant thermal neutron capture cross-section, and the transmutation products of Gd have a significantly large capture cross-section, making it an excellent neutron-absorbing material. The transmutation product of Gd is ($^{154}_{64}$Gd → $^{155}_{64}$Gd → $^{156}_{64}$Gd → $^{157}_{64}$Gd → $^{158}_{64}$Gd → $^{159}_{64}$Gd → $^{160}_{64}$Gd) Gd – one of the most effective neutron absorbent and the main alloying element of Mg alloys [23–26]. The binary phase diagram of Mg–Gd shows an eutectic phase with a solubility of 23.5 wt% Gd at the eutectic temperature of 548°C and 3.8 wt% Gd at 200°C. Mg–Gd-based alloys tend to form supersaturated solid solutions during solidification; this new strengthening precipitate readily forms following heat treatment. Therefore, Mg–Gd alloy becomes a material with excellent neutron absorption capacity. Hence, an innovative rare-earth Mg alloy material for neutron-shielding was designed, and Gd, an alloying element with both effective neutron-shielding and high solid

solubility, was selected for this study. Theoretically, some problems caused by the composition design of some current metal-based materials have been avoided; for example, metal-based materials with added boron cannot exhibit both high shielding efficiency and excellent mechanical properties. The thermal neutron-shielding properties of the prepared metallic materials were tested using a 252Cf source, with the attenuation ratio of the sample obtained by simulation using SuperMC Monte Carlo software, which verified the high neutron-shielding efficiency of the Mg–Gd alloy. The effect of radiation on the microstructural evolution of the Mg–Gd alloy was further studied using 6 MeV Au ion irradiation to simulate neutron irradiation at 473 K temperature, with the radiation resistance of the Mg–Gd alloy evaluated. Currently, reports on rare-earth Mg alloy radiation-shielding materials remain limited, thus highlighting the novelty of this study. The results of this study may provide direction for future research on multi-rare-earth Mg alloy shielding materials.

2 Materials and methods

2.1 Materials

Three compositions of binary as-cast Mg–Gd alloys with Gd contents of 5, 10, and 15% were designed, along with a control group of pure Mg alloy. The experimental materials consisted of a pure Mg ingot (99.95%) and a Mg–30Gd master alloy. Melting was performed in a resistance furnace within a heat-resistant mild steel crucible under a protective gas environment composed of 99% CO_2 and 1% SF_6. Subsequently, the molten mixture was poured into a preheated steel mold at a temperature of 500°C, following an isothermal holding time of 15 min. The chemical composition of the designed alloys was detected by the X-ray fluorescence spectrometer. The related results are listed in Table 1. The contents of alloying elements were consisted with the design.

Table 1: Chemical composition of Mg–*x*Gd

Sample	Mg (wt%)	Gd (wt%)
Pure Mg	99.71	—
Mg–5Gd	95.31	4.11
Mg–10Gd	91.09	8.75
Mg–15Gd	84.47	14.12

2.2 Irradiation experiment

Slabs measuring 150 mm × 150 mm × 4 mm were obtained from the pure Mg, Mg–5Gd, Mg–10Gd, and Mg–15Gd ingots for conducting neutron shielding performance tests at the Beijing Research Center for Radiation Application. The experiment utilized a ^{252}Cf neutron source with an emission rate of 8.2×10^7 s^{-1} installed within a collimator made of polyethylene and featured a collimation aperture diameter of φ10 cm. The fast neutrons emitted by the ^{252}Cf source were moderated effectively to form a thermal neutron field. The neutrons were detected using a ^{3}He proportional counter.

Irradiation experiments were conducted at the Institute of Nuclear Science and Technology, Sichuan University, Chengdu, China, using a 2 × 3 MV tandem accelerator [9]. The dimensions of the samples used for the irradiation were 5 mm × 5 mm × 0.5 mm. A focused ion beam (FIB) technique was employed to prepare cross-sectional transmission electron microscopy (TEM) specimens for Au-ion irradiation. The Au-ion irradiation was conducted at a temperature of 200°C, reaching a fluence of approximately 1.25×10^{16} Au/cm^2, with the energy of Au^+ set at 6 MeV.

2.3 SuperMC (Monte Carlo N particle transport code)

SuperMC is a software program that employs the Monte Carlo method to compute the transport phenomena associated with neutrons, photons, and electrons within intricate three-dimensional geometrical structures [27]. Figure 1(a) illustrates the SuperMC model, which accurately represents the experimental conditions for evaluating neutron shielding performance [28]. Figure 1(b) illustrates the neutron source utilized for both simulation and experimentation. Using a^{252}Cf source, neutrons were guided through a collimator with a cross-sectional diameter of 100 mm to generate a neutron field. This collimated field was further modified by incorporating paraffin neutron moderators within the fillings of the collimation apertures, which induced the formation of a thermal neutron field. The Mg–*x*Gd sample was placed on the other side of the collimator to simulate the actual experimental setup. The radiation field was established along the central axis and positioned 1,580 mm from the radiation source. A counting sphere was set up on the center axis of the radiation field, 1,580 mm from the source, with the neutron flux through the counting surface recorded to obtain information on the neutron flux with and without the added sample.

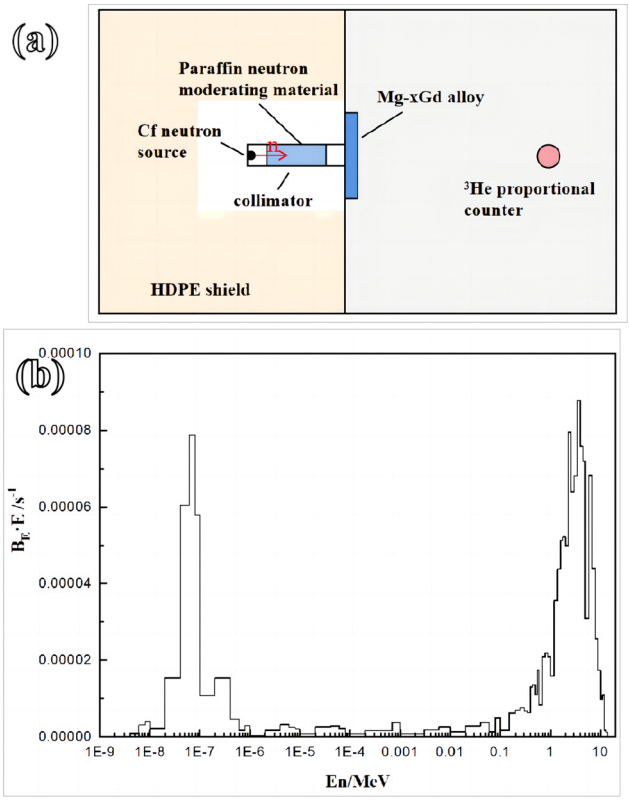

Figure 1: (a) SuperMC model; and (b) neutron sources for simulation.

2.4 Characterizations

After polishing and etching, the microstructure of the alloy was examined using optical metallography. Scanning electron microscopy (SEM) was used to investigate the distribution and size of the alloys. Tensile testing was conducted at room temperature (RT) using a standard tensile testing machine with a strain rate of 1.7×10^{-3} s^{-1} to obtain the yield strength (YS), tensile strength (UTS), and elongation (FE) of the alloy. TEM was used to analyze the phase structure and morphology of the post-irradiation material. Sub-100-nm thin specimens were prepared using an FIB lift-out technique with an FIB/SEM instrument. During the TEM sample preparation, thin Pt layers were deposited to protect against FIB gallium contamination. An aberration-corrected JEOL2100F TEM/STEM operating at 200 keV was used to characterize the FIB foils through conventional bright-field and dark-field techniques.

3 Results

3.1 Microstructure

The microstructures of the as-cast Mg–Gd alloys are shown in Figures 2 and 3. According to existing research, the alloy

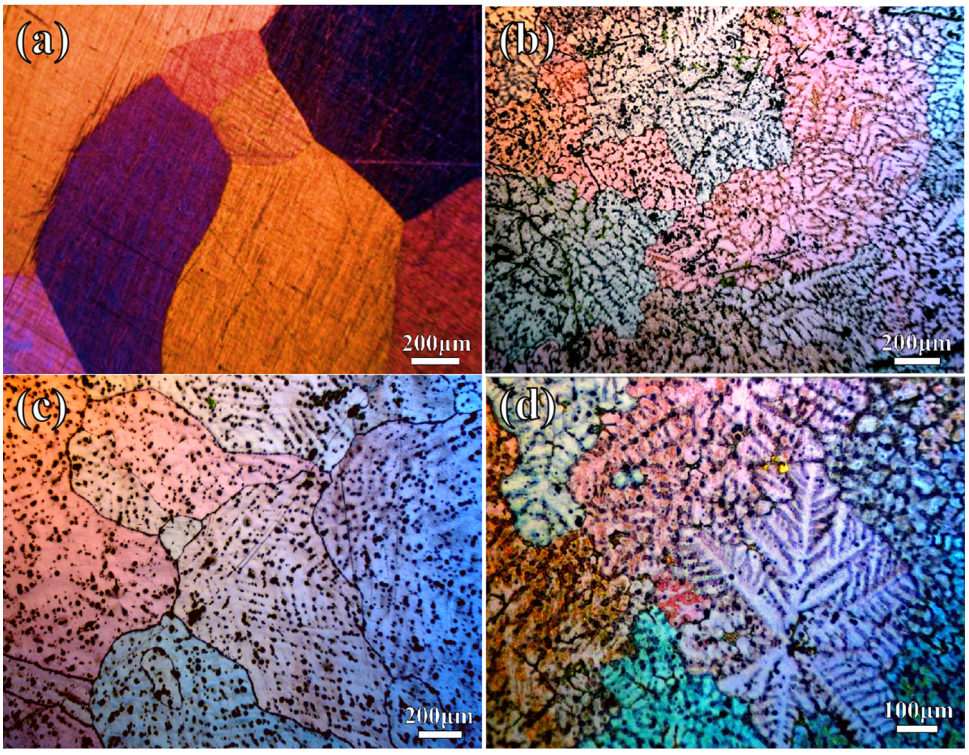

Figure 2: OM of Mg alloy: (a) pure Mg, (b) Mg–5Gd, (c) Mg–10Gd, and (d) Mg–15Gd.

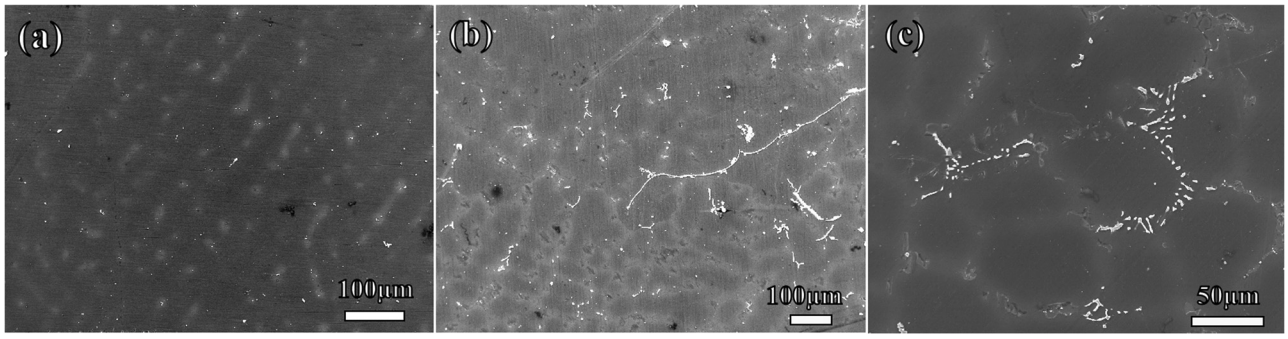

Figure 3: SEM of Mg alloy: (a) Mg–5Gd, (b) Mg–10Gd, and (c) Mg–15Gd.

structure of as-cast Mg–Gd alloys with different Gd content is primarily composed of α-Mg and eutectic phases (α-Mg + Mg_5Gd), along with some non-equilibrium solidified Mg_3Gd phases [29,30]. As the Gd content increases, the number of precipitated Mg_5Gd phases gradually increases, and the morphology changes. Upon increasing the Gd content from 5 to 10%, a notable transition in the morphology of the Mg_5Gd phase was observed, shifting from a granular structure (Figures 2(b) and 3(a)) to a skeletal morphology (Figures 2(c) and 3(b)), accompanied by a reduction in grain size compared to pure Mg. In the context of non-equilibrium solidification, the Mg–15Gd alloy displayed a dendritic morphology attributed to Gd segregation in the as-cast state (Figures 2(d) and 3(c)), with the Mg_5Gd phase distributed in a discontinuous reticular pattern along the interdendritic regions. The average grain sizes of Mg–5Gd, Mg–10Gd, and Mg–15Gd alloys are, respectively, 270, 170, and 140 μm.

3.2 Mechanical properties

Table 2 presents the YS, UTS, and FE of pure Mg and the as-cast Mg–Gd alloys at RT. When comparing the Mg–*x*Gd (x = 0, 5, 10, and 15 wt%) alloys, we observe a significant increase in both YS and UTS as the percentage of Gd in the alloys increased from 5 to 15%. The Mg–15Gd alloy exhibited a UTS of 142.2 MPa, a substantial improvement over the 67.6 MPa of the Mg–5Gd alloy. Similarly, the YS of the Mg–15Gd alloy matches that of the Mg–5Gd alloy, both at 91.7 MPa, reflecting a notable increase from the initial 33.4 MPa in the Mg–5Gd alloy. However, the plasticity of the alloys follows a different change rule. Initially, as the Gd content increased, the elongation decreased from 2.9% for the Mg–5Gd alloy to 1.3% for the Mg–10Gd alloy. However, with a further increase in the Gd content of the Mg–15Gd alloy, the elongation partially recovered, reaching 1.8%.

3.3 Neutron shielding properties

The neutron shielding efficacy of the alloy was assessed by the neutron decay ratio, which is defined as the ratio of I_0 to I; I_0 represents the count obtained without any shielding material, and I represents the count after the shielding material is introduced. Table 3 presents the comparative analysis of the experimental and simulation results. The results obtained under the same conditions demonstrated remarkable consistency between the neutron decay ratios obtained through experimental observation and SuperMC simulation. The neutron decay rate obtained by these two methods was consistent with the variation trend of the Gd content. Notably, compared with pure Mg, introducing Gd significantly alters the thermal neutron attenuation characteristics of the alloy and enhances its shielding properties.

The deviations between the experimental tests and simulations were less than 10%, with the thermal neutron calculation results generally smaller than the experimental results, attributed to the following reasons: the simulation calculation was performed under ideal conditions, ignoring the influence of neutron reflection and scattering in the surrounding environment. In the theoretical calculation model, the elements in the material are evenly distributed in space. However, in the as-cast Mg–Gd alloy, the microscopic distribution is not uniform. Specifically, as the thermal neutron effective absorption element Gd increased, it accumulated more at the grain boundaries and formed a second phase.

Table 2: Tensile mechanical properties of as-cast alloys

Sample	YS (MPa)	UTS (MPa)	FE (%)
Pure Mg	10.2	65.5	6.1
Mg–5Gd	33.4	67.6	2.9
Mg–10Gd	59.3	83.8	1.3
Mg–15Gd	91.7	142.2	1.8

Table 3: Experimental and SuperMC simulated thermal neutron attenuation ratio

	Mg	Mg–5Gd	Mg–10Gd	Mg–15Gd
Experiment	1.03	8.44	12.97	22.33
SuperMC	1.04	7.60	13.48	20.18

This uneven distribution may lead to changes in the shielding properties of the alloy in different regions.

3.4 Ion irradiation

Figure 4 shows the TEM micrographs near the [01 $\bar{1}$ 0] zone axis of the Mg–15Gd alloy after Au ion irradiation, with diffraction vectors g = [0002] and g = [$\bar{2}$110]. The visibility of dislocation loops under different diffraction vectors can be identified *via* TEM, where Burgers vectors 1/3 ⟨11$\bar{2}$0⟩ ⟨c + a⟩ and 1/6 ⟨20$\bar{2}$3⟩ ⟨c⟩ dislocation loops [31–34], as well as some small dislocations, are represented by yellow circles, blue circles, and red dashed lines. The evolution of the irradiation defects was strongly correlated with the c/a ratio, solute atoms, and irradiation dose [35,36]. Increasing the Gd solute concentration promoted the formation of basal plane defects in the Mg matrix. The solute likely lowers the stacking fault energy, leading to the formation of more basal-plane dislocations [37]. However, the origin of dislocation loops, whether from interstitial atoms or vacancy evolution, cannot be determined at present.

Figure 5 shows the nanoscale Gd-rich precipitates induced by irradiation in the Mg matrix and secondary phases. The precise composition of these precipitates is listed in Table 4, which suggests that the precipitate could be the $Mg_{45.9}Gd_{9.08}$ phase. An in-depth examination of the intricate phase relationships between the second phase and granular precipitates is presented in Figure 6(b). A superlattice structure is observed in the electron diffraction pattern, with $(111)_{Mg3Gd}$ parallel to $(111)_{Mg45.9Gd9.08}$ and $(220)_{Mg3Gd}$ parallel to $(220)_{Mg45.9Gd9.08}$. Additionally, Figure

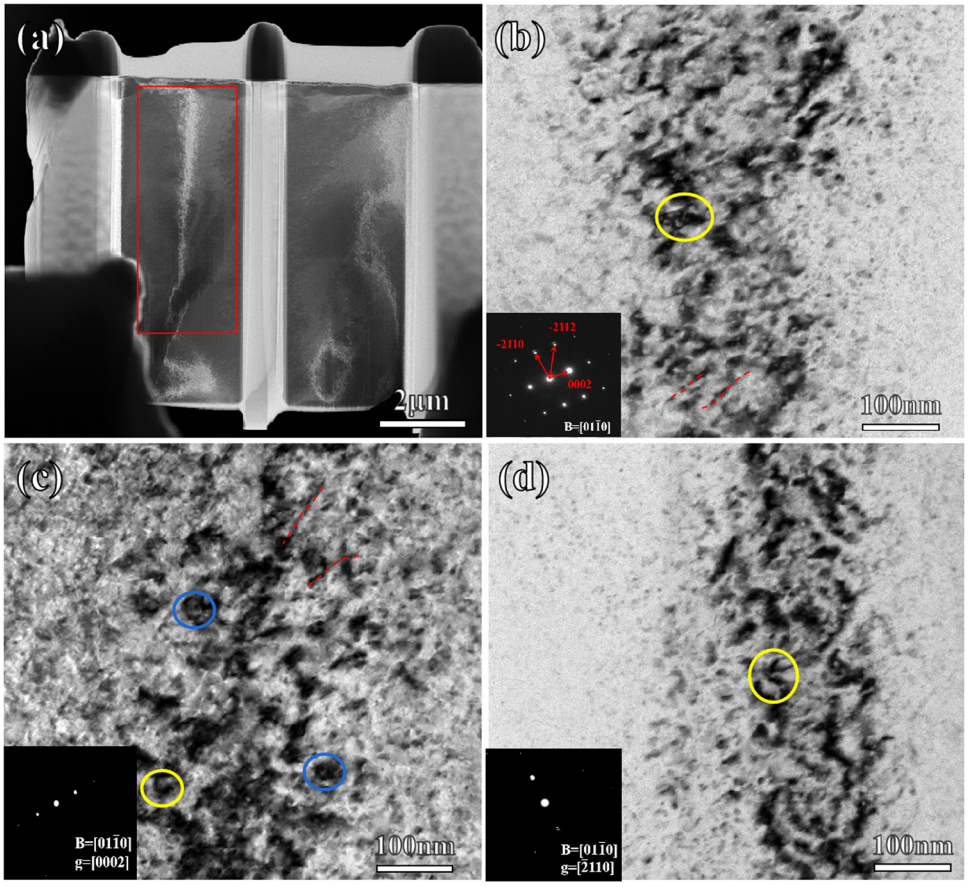

Figure 4: TEM micrographs, under different diffraction vectors, near the [01$\bar{1}$0] zone axis, depicting the microstructure of Mg–15Gd alloy after Au ion irradiation. (a) Target area within the red box on the FIB sample. (b) Along the [01$\bar{1}$0] zone axis. (c) g = [0002]. (d) g = [$\bar{2}$110]. Yellow and blue circles represent ⟨c + a⟩ and ⟨c⟩ dislocation loops; the red dashed line indicates some uncollected point defects.

6(a) shows the irradiation-induced defects in the second phase, with a small number of dislocation loops observed at the edges. These defects were formed along the (001) plane, demonstrating a distinct regularity.

In the FCC structure, close-packed planes exhibited the lowest surface energies. Hence, during irradiation, oversaturated vacancies preferentially aggregate along the {111} planes, forming vacancy clusters [38]. When these clusters attain sufficient size, the unstable crystal planes on both sides collapse, forming dislocation loops. Concurrently, the dislocation loops in the matrix may originate from the aggregation of point defects generated by cascade collisions during irradiation.

Table 4: EDS of (a) granular phase and (b) leaf-like phase in Figure 4

Phases	Mg (at.%)	Gd (at.%)
Granular phase	89.73	10.27
Willow leaf phase	84.25	15.75

Remarkably, even at a high dose of 10 dpa, the alloy did not exhibit a significant number of voids, highlighting its excellent radiation resistance attributed to the substantial amount of FCC phases present in the alloy [39]. When ions interact with these Gd-containing phases within the FCC structure, the displaced atoms move along interstitial

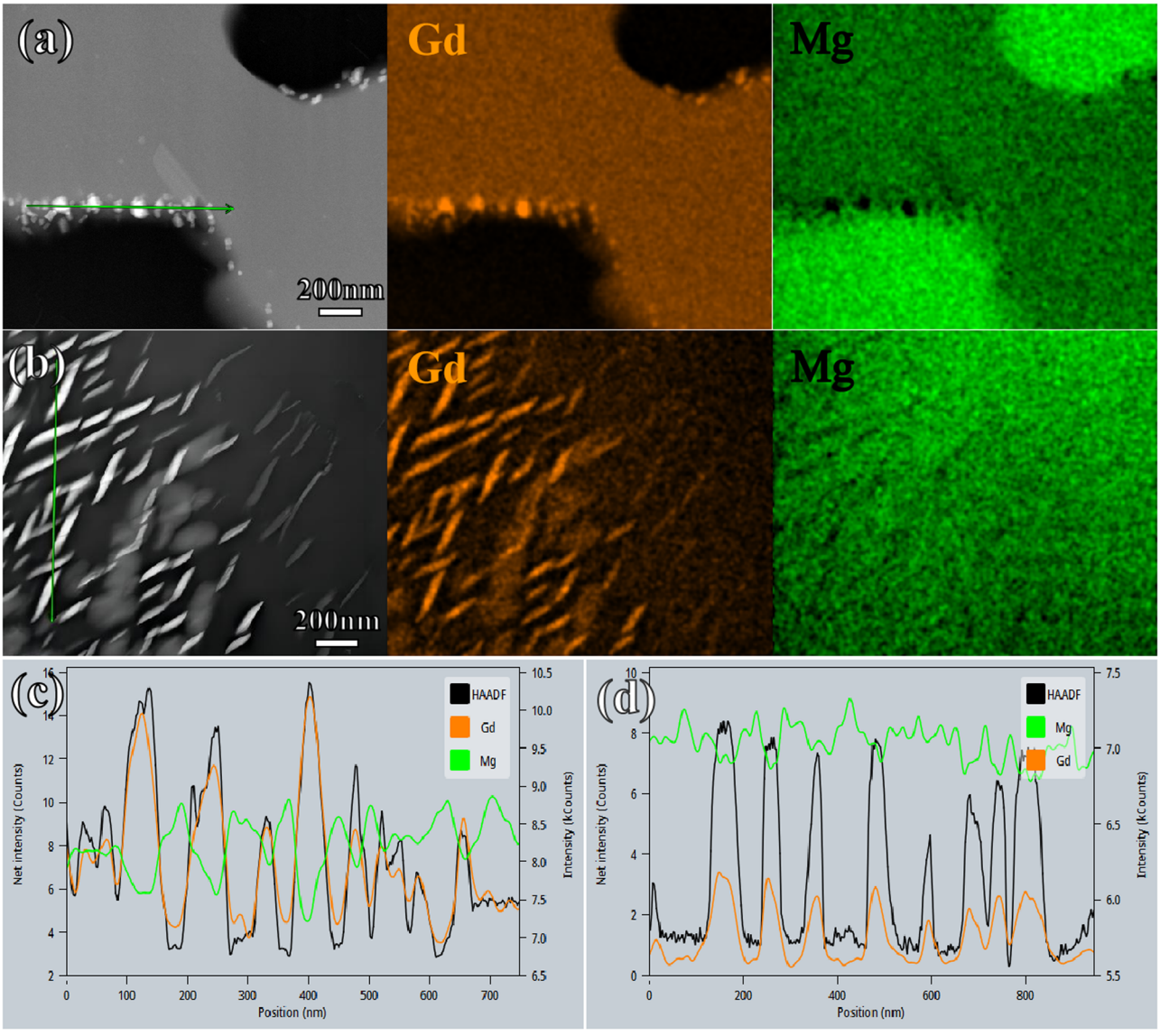

Figure 5: (a) Granular Gd-rich phase precipitated in the second phase. (b) Leaf-like Gd-rich phase precipitated in the matrix. EDS line scan of the (c) granular and (d) leaf-like phases.

paths in the close-packed crystal directions ⟨110⟩ increasing the cascade collision distances. This phenomenon, known as the "channeling effect," inhibits the generation of point defects, thereby enhancing the overall stability of the alloy under irradiation.

In contrast, atoms traveling along other FCC crystallographic directions within the Mg matrix undergo "focusing collisions" following the initial collision [40,41]. These focusing collisions progressively diminished the scattering angles for each displaced atom in a specific crystal direction, thereby facilitating energy transfer. Notably, these collisions occurred predominantly in the close-packed directions, and the hexagonal close-packed structure of the Mg alloy augmented these interactions. Consequently, the displaced atoms experience increased energy losses, leading to a reduction in defect generation.

Furthermore, void formation is intricately linked to temperature variations. The aggregation of vacancies and self-interstitial atoms during cascade collisions within the FCC crystal structure influences the emergence of voids in the Mg_5Gd phase, which become discernible *via* TEM only at temperatures surpassing approximately 0.35 times the material's melting point (T_m) [42]. Additionally, given the higher melting point of the Mg_5Gd phase, no void formation was observed during irradiation at 200°C. These temperature-dependent void-formation characteristics highlight the unique behavioral responses of the alloy under varying conditions.

Finally, the emerging dislocations served as conduits for atomic diffusion, providing an auxiliary driving force that propelled the precipitation of Gd-containing phases with particle or leaf-like morphologies.

4 Discussion

4.1 Strengthening mechanism of mechanical properties

The strengthening mechanism of Mg alloys at room temperature involves solid-solution strengthening, grain refinement strengthening, and second-phase strengthening. The improvement in the strength of the as-cast Mg–Gd alloy was mainly attributed to second-phase strengthening and grain refinement. The eutectic phase β-Mg_5Gd typically precipitates parallel to the $\{10\,\bar{1}\,0\}_\alpha$ on the grain boundaries of the as-cast structure, while the precipitated plates formed on the prism planes of the Mg matrix act as effective barriers hindering dislocation movement and twin expansion. Increasing the number of precipitated phases resulted in stronger strengthening effects.

The grain refinement by Gd partially originates from the influence of Mg_5Gd on heterogeneous nucleation. The interface energy between the nucleation substrate and crystalline phase determines the heterogeneous nucleation ability, with the mismatch between the substrate and crystalline phase being a key factor in determining the interface energy. The mismatch between the Mg_5Gd phase (111) plane and the α-Mg phase $(10\bar{1}0)$ plane can reach 5.8% [43], making it an extremely effective nucleation core for the α-Mg phase, thus hindering its growth. The alloy underwent metal mold casting, which resulted in a rapid cooling rate of the alloy liquid. Under non-equilibrium crystallization conditions, solute Gd is influenced by its own segregation, leading to its enrichment at the forefront of the

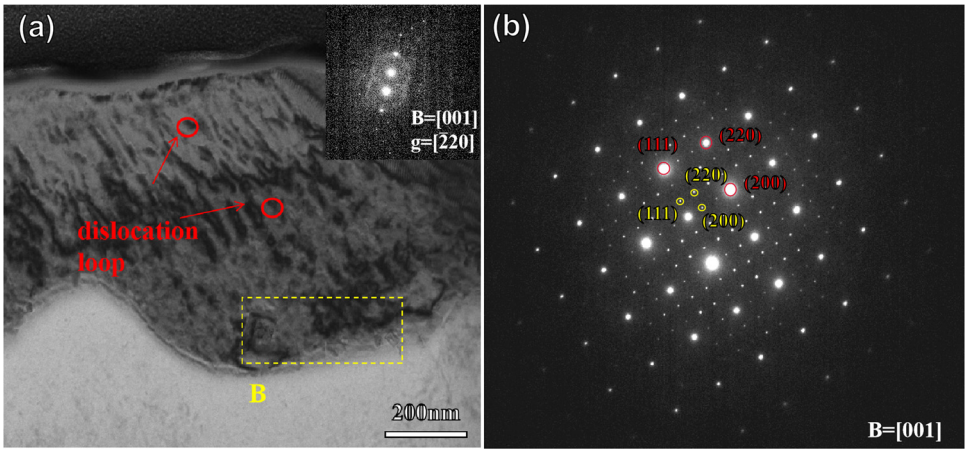

Figure 6: (a) Observation of dislocations in the second phase along the [001] axis. (b) Electron diffraction pattern of the yellow area in the second phase containing granular precipitates.

solid–liquid crystallization interface, preventing sufficient diffusion and increasing the undercooling of the melt. Additionally, numerous Mg_5Gd phases distributed at the grain boundaries further hinder the diffusion of liquid phase atoms into the solid phase, inhibiting grain growth [44]. Furthermore, the chemical properties of Gd effectively increase the surface tension at the solid–liquid interface, reducing the critical nucleation radius and facilitating nucleation, thereby significantly refining the microstructure of the as-cast alloy.

However, as the Gd content increased, several dendritic structures were internally generated in the alloy, leading to stress concentration. This stress concentration results in a distinctly brittle fracture behavior, which exerts a certain embrittling effect on the matrix and reduces the plasticity of the alloy. Consequently, the plasticity of the alloy was lower than that of pure Mg.

4.2 Effect of Gd on thermal neutron shielding performance

The enhancement of neutron shielding performance of the alloy with increasing Gd content can be attributed to two main factors, as inferred from the simulation and experimental results: (1) Adding effective absorptive elements alters the macroscopic absorption cross-section of the material. Gd possesses a significantly larger thermal neutron absorption cross-section (approximately 49,000 b) compared to that of Mg (0.04 b) [45]. (2) The microstructure of Mg alloys affects their neutron-shielding efficiency. The alloy grains were noticeably refined, and the number of Gd-containing phases increased in both the grain interiors and grain boundaries. Generally, the neutron absorption efficiency of a material increases as the mean free path of neutrons decreases. A reduced neutron mean free path signifies a higher probability of collisions between neutrons and atoms within the same material thickness; in other words, neutrons can be effectively absorbed by atoms over a shorter distance. The refinement of the alloy grains and the increase in precipitated phases reduced the distance between the Gd-containing phases, leading to a more uniform distribution, an increased probability of collisions between neutrons and Gd, and a decrease in the mean free path.

5 Conclusion

In summary, incorporating Gd in the 0–15 wt% range significantly enhances the thermal neutron absorption capability, along with notable increases in tensile and YS of Mg alloys. The as-cast Mg–15Gd alloy exhibited good radiation tolerance under Au ion irradiation at 200°C and 10 dpa. The presence of 1/6 $\langle 20\bar{2}3\rangle$ $\langle c\rangle$ and 1/3 $\langle 11\bar{2}0\rangle$ $\langle c + a\rangle$ dislocation loops was observed in the matrix. Irradiation-induced nanoscale leaf-like Gd-rich precipitates were identified in the matrix, while granular Gd-rich phases were identified in the primary phase. Irradiation did not induce void formation in the alloy, primarily because of the influence of the nanoscale Mg_5Gd precipitates and their interaction with the matrix structure during cascade collisions. With further studies of radiation effects in the future, we believe that Mg–Gd-based alloys will exhibit potential in terms of shielding efficiency and radiation resistance.

Acknowledgments: The authors are grateful to Dr. Zhu Changda from Sichuan University for his support techniques and guidance in radiation experiments. The authors thank the Joint Lab for Electron Microscopy of Chongqing University and the Analytical and Testing Center of Chongqing University.

Funding information: This work was funded by Key Research and Development Plan of Sichuan Province (24QYCX0537).

Author contributions: All authors have accepted responsibility for the entire content of this manuscript and approved its submission.

Conflict of interest: The authors state no conflict of interest.

Data availability statement: The datasets generated during and/or analyzed during the current study are available from the corresponding author on reasonable request.

References

[1] Dittmar MJE. Nuclear energy: Status and future limitations. Energy. 2012;37(1):35–40.
[2] Uğur FA. New applications and developments in the neutron shielding. EPJ Web of Conferences. EDP Sciences; 2017. p. 01022
[3] Hoffelner W. Mechanical properties of nuclear materials. In: Hoffelner W, editor. Materials for Nuclear Plants: From Safe Design to Residual Life Assessments. London: Springer; 2013. p. 197–254.
[4] Zinkle SJ, Was GS. Materials challenges in nuclear energy. Acta Mater. 2013;61(3):735–58.
[5] Zinkle SJ, Busby JT. Structural materials for fission & fusion energy. Mater Today. 2009;12(11):12–9.
[6] Halliwell E, Couch C, Begum R. Increase in linear attenuation coefficient by changing crystal structure of materials for radiation shielding and biomedical devices safety. Colloid Surface A. 2021;622:126646.

[7] Saeed A. Developed borated austenitic stainless steel alloys as nuclear reactor control rods. Nucl Eng Des. 2023;413:112515.
[8] Xu ZG, Jiang LT, Zhang Q. The design of a novel neutron shielding B_4C/Al composite containing Gd. Mater Design. 2016;111:375–81.
[9] Sun WQ, Yu XH. Study on a high-boron-content stainless steel composite for nuclear radiation. Materials. 2021;14:7004–8.
[10] Merklein M, Wieland M, Lechner M. Hot stamping of boron steel sheets with tailored properties: A review. J Mater Process Tech. 2016;228:11–24.
[11] Rotkovich AA, Tishkevich DI, Bondaruk AA, German SA, Razanau IU, Zubar TI, et al. Epoxy-w composite materials: microstructure, structure, and radiation efficiency. Adv Phys Res. 2023;5(3):133–45.
[12] Dong M, Zhou S, Xue X, Feng X, Yang H, Sayyed MI, et al. Upcycling of boron bearing blast furnace slag as highly cost-effective shield for protection of neutron radiation hazard: An innovative way and proposal of shielding mechanism. J Clean Prod. 2022;355:131817.
[13] Jian S, Zhu HY, Wang WS, Duan YQ. Effect of boron segregation on the surface crack of low carbon boron-bearing steel. Results Phys. 2012;2:089–101.
[14] Shang Y, Yang G, Su FM. Multilayer polyethylene/hexagonal boron nitride composites showing high neutron shielding efficiency and thermal conductivity. Compos Commun. 2020;3:7–12.
[15] Liu XC, Li XJ, Li ZX, Wang XH. Influence of heavy concrete on seismic response of transfer and purging rooms of nuclear power plant. Structures. 2023;51:1372–83.
[16] García Gallardo JA, Giménez MAN, Gervasoni JL. Nuclear properties of Tungsten under 14 MeV neutron irradiation for fusion-fission hybrid reactors. Ann Nucl Energy. 2020;147:107739.
[17] Tishkevich DI, Rotkovich AA, German SA, Zhaludkevich AL, Vershinina TN, Bondaruk AA, et al. Heavy alloy based on tungsten and bismuth: fabrication, crystal structure, morphology, and shielding efficiency against gamma-radiation. Rsc Adv. 2023;13(35):24491–98.
[18] Al-Shelkamy SA, Vega-Carrillo HR, Xie Z, El-Hossary FM, Mosa ES, Mahdy AA, et al. Mechanical and radiation shielding characterization of W-based alloys for advanced nuclear unit. Appl Radiat Isotopes. 2023;201:110995.
[19] Wang JQ, Qin XZ, Cheng SH. The microstructure and mechanical performance optimization of a new Fe-Ni-based super alloy for Gen IV nuclear reactor: The critical role of Nb alloying strategy. Mater Charact. 2023;205:113240.
[20] Wharry JP, Clement CD, Zhao Y, Baird K, Frazer D, Burns J, et al. Mechanical testing data from neutron irradiations of PM-HIP and conventionally manufactured nuclear structural alloys. Data in Brief. 2023;48:109092.
[21] Zhang P, Li J, Wang WX, Tan XY, Xie L, Chen XP. Design, shielding mechanism and tensile property of a novel (B_4C + 6061Al)/Cf/6061Al laminar neutron-shielding composite. Vacuum. 2020;177:109383.
[22] Sturcken EF. Irradiation effects in magnesium and aluminum alloys. J Nucl Mater. 1979;82(1):39–53.
[23] Zheng J, Yan ZM, Ji JS. Effect of heat treatment on mechanical properties and microstructure evolution of Mg-9.5Gd-4Y-2.2Zn-0.5Zr alloy. J Magnes Alloys. 2022;10(4):1124–32.
[24] Wan S. 155/157Gd areal density: a model for design and fabrication of Gd_2O_3/316L novel neutron shielding composites. Vacuum. 2020;89:102–9.
[25] Liu K, Hu DL, Lou F. Effects of deformation temperatures on microstructures, aging behaviors and mechanical properties of Mg-Gd-Er-Zr alloys fabricated by hard-plate rolling. J Magnes Alloys. 2022;10(2):049–53.
[26] Liu LZ, Chen XH, Pan FS. A review on electromagnetic shielding magnesium alloys. J Magnes Alloys. 2021;9(6):1906–21.
[27] Wu YC, Song J, Hu LQ. Super Monte Carlo Simulation Program for Nuclear and Radiation Process: SuperMC. Nucl Sci Eng. 2016;36(1):62–71.
[28] Qi ZD, Yang Z, Meng XF, Yang XG, Liang MX, Li CY, et al. Microstructure, thermophysical properties and neutron shielding properties of Gd/316L composites for spent nuclear fuel transportation and storage. Mater Today Commun. 2023;37:107315.
[29] Verbovytskyy Y, Gonçalves AP. On the ternary $RE_xMg_{1-x}Al_2$ (RE = Gd-Tm), $RE_3Ag_{5\pm x}Mg_{11\pm x}$, $REAg_{4+x}Mg_{2-x}$, $RE_4Ag_{10.3}Mg_{12}$ and $RE_4Ag_{10+x}Mg_{3-x}$ (RE = Ce-Nd, Sm) phases. Solid State Sci. 2015;40(8):4–91.
[30] Tong X, Zai L, You G, Wu H, Wen H, Long S. Effects of bonding temperature on microstructure and mechanical properties of diffusion-bonded joints of as-cast Mg–Gd alloy. Mat Sci Eng A-Struct. 2019;767:138408.
[31] Xu WZ, Zhang YF, Cheng GM, Jian WW, Millett PC, Koch CC, et al. Dynamic void growth and shrinkage in mg under electron irradiation. Mater Res Lett. 2014;2(3):176–83.
[32] Khan AK, Yao Z, Daymond MR. Effect of foil orientation on damage accumulation during irradiation in magnesium and annealing response of dislocation loops. J Nucl Mater. 2012;423(1-3):132–41.
[33] Wu S, Cao C, Bo H. In-situ atomic-scale observation the escape of irradiation-induced dislocation loops in magnesium. J Alloy Compd. 2022;895:162708.
[34] Xu W, Zhang Y, Cheng G. On the origin and behavior of irradiation-induced c-component dislocation loops in magnesium. Acta Mater. 2017;131:457–66.
[35] Khan AK, Yao Z, Daymond MR, Holt RA. Irradiation damage in commercial purity magnesium. Nucl Instrum Meth B. 2012;272:231–5.
[36] Griffiths M. Evolution of microstructure in hcp metals during irradiation. J Nucl Mater. 1993;205:225–41.
[37] Geng J, Chisholm MF, Mishra RK, Kumar KS. The structure of $\langle c + a \rangle$ type dislocation loops in magnesium. Phil Mag Lett. 2014;94(6):377–86.
[38] Osetsky YN, Bacon DJ, Serra A, Singh BN, Golubov SI. Stability and mobility of defect clusters and dislocation loops in metals. J Nucl Mater. 2000;276(1–3):53–77.
[39] Bacon DJ, Gao F, Osetsky YN. The primary damage state in fcc, bcc and hcp metals as seen in molecular dynamics simulations. J Nucl Mater. 2000;276(1–3):1–12.
[40] Silsbee RH. Focusing in collision problems in solids. J Appl Phys. 1957;28(11):1246–50.
[41] Leibfried G. Defects in dislocations produced by focusing collisions in fcc lattices. J Appl Phys. 1960;31(1):117–21.
[42] Singh BN, Evans JH. Significant differences in defect accumulation behaviour between fcc and bcc crystals under cascade damage conditions. J Nucl Mater. 1995;226(3):277–85.
[43] Gao X, He SM, Zeng XQ, Peng LM, Ding WJ, Nie JF. Microstructure evolution in a Mg–15Gd–0.5 Zr (wt.%) alloy during isothermal aging at 250°C. Mat Sci Eng A-Struct. 2006;431(1–2):322–7.
[44] Guan K, Egusa D, Abe E, Zhang J, Qiu X, Yang Q, et al. Microstructures and mechanical properties of as-cast Mg-Sm-Zn-Zr alloys with varying Gd contents. J Magnes Alloys. 2022;10(5):1220–34.
[45] Zhang P, Li J, Wang WX, Tan XY, Xie L, Guo FY. The design, microstructure and mechanical properties of a novel Gd_2O_3/6061Al neutron shielding composite. Vacuum. 2019;162:92–100.